Lipids in Health and Disease

RESEARCH

Open Access

Rod-shaped mesoporous silica nanoparticles reduce bufalin cardiotoxicity and inhibit colon cancer by blocking lipophagy

Yibao Fan[1,2,3], Wei Zhang[1,3], Zoya Iqbal[4], Xinxin Li[4], Zhiyin Lin[2], Zhuolin Wu[2], Qianyou Li[2], Hongxia Dong[5], Xianbin Zhang[1,3], Peng Gong[1*] and Peng Liu[1*]

Abstract

Background Bufalin (BA) is a potent traditional Chinese medicine derived from toad venom. It has shown significant antitumor activity, but its use is limited by cardiotoxicity, which necessitates innovative delivery methods, such as rod-shaped mesoporous silica nanoparticles (rMSNs). rMSNs have been extensively employed for reducing drug toxicity and for controlled or targeted drug delivery in tumor therapy. However, their potential in delivering BA has not been completely elucidated. Therefore, in this study, BA-loaded rMSNs (BA-rMSNs) were developed to investigate their potential and mechanism in impairing colon cancer cells.

Methods rMSNs were developed via the sol–gel method. Drug encapsulation efficiency and loading capacity were determined to investigate the advantages of the rMSN in loading BA. The antiproliferative activities of the BA-rMSNs were investigated via 5-ethynyl-2′-deoxyuridine and CCK-8. To evaluate cell death, Annexin V-APC/PI apoptotic and calcein-AM/PI double staining were performed. Western blotting, oil red O staining, and Nile red solution were employed to determine the ability of BA-rMSNs to regulate lipophagy.

Results The diameter of the BA-rMSNs was approximately 60 nm. In vitro studies demonstrated that BA-rMSNs markedly inhibited HCT 116 and HT-29 cell proliferation and induced cell death. In vivo studies revealed that BA-rMSNs reduced BA-mediated cardiotoxicity and enhanced BA tumor targeting. Mechanistic studies revealed that BA-rMSNs blocked lipophagy.

Conclusions rMSNs reduced BA-mediated cardiotoxicity and impaired the growth of colon cancer cells. Mechanistically, antitumor activity depends on lipophagy.

Keywords Bufalin, Mesoporous silica, Rod shape, Lipophagy, Colon cancer

*Correspondence:
Peng Gong
doctorgongpeng@szu.edu.cn
Peng Liu
surgeonliupeng@126.com
[1]Department of General Surgery, Institute of Precision Diagnosis and Treatment of Digestive System Tumors and Guangdong Provincial Key Laboratory of Chinese Medicine Ingredients and Gut Microbiomics, Carson International Cancer Center, Shenzhen University General Hospital, Shenzhen University, Shenzhen, Guangdong 518055, China
[2]School of Pharmacy, Shenzhen University Medical School, Shenzhen University, Shenzhen, Guangdong 518060, China
[3]International Association for Diagnosis and Treatment of Cancer, HongKong, Guangdong 999077, China
[4]Department of Gastrointestinal Surgery, The First Affiliated Hospital of Shantou University Medical College, Shantou, Guangdong 515041, China
[5]Department of Gastroenterology, General Hospital of Chinese PLA, Beijing 100853, China

Introduction

Colon cancer is the most common type of gastrointestinal cancer [1]. In 2024, it accounted for 9.6% of new cases and 9.3% of deaths, making it the primary cause of cancer incidence and mortality among gastrointestinal cancers [2]. Despite the significant improvement in the early diagnosis of colon cancer in recent years, nearly one-quarter of patients continue to be diagnosed at later stages of the disease [3]. For these patients, chemotherapy remains the primary treatment. However, chemotherapy, such as 5-fluorouracil, oxaliplatin, and irinotecan, only slightly improves patient survival. Thus, developing novel therapeutic strategies is essential for colon cancer patients.

Bufalin (BA) is a monomeric compound in Chansu, the dried secretions from the parotoid gland of the Asian common toad [4]. Chen et al. reported that, compared with oxaliplatin, BA could significantly inhibit tumor cell growth and enhance the antitumor effects of chemotherapy [5]. However, BA and digoxin have similar chemical structures and exhibit significant cardiotoxic effects. Ko et al. reported that the consumption of 100 mL of tea containing Chansu resulted in acute cardiotoxicity and led to death within two hours [6].

Nanocarrier-mediated drug delivery has demonstrated an advantage in reducing drug toxicity. It enhances drug targeting to tumors and substantially reduces drug accumulation in the heart, liver, and kidneys. Mesoporous silica nanoparticles (MSNs) have a unique porous structure and are widely used in drug delivery. MSNs enhance drug deposition in tumors through the enhanced permeability and retention (EPR) effect. Furthermore, the high porosity of MSNs significantly enhances their specific surface area. This improves their drug loading capacity and delivery efficiency compared with those of common inorganic nanomaterials [7, 8]. Additionally, MSNs have good biocompatibility and minimal cytotoxicity [9–12].

Interestingly, previous studies have suggested that the shape of nanoparticles influences delivery efficiency [13–15]. Compared with round-shaped and flaky-shaped nanoparticles, rod-shaped MSNs (rMSNs) exhibit greater cellular internalization. For example, Banerjee et al. demonstrated that rMSNs exhibited greater mucus and intestinal epithelial barrier penetration than did spherical rMSNs [16]. These findings indicate that the use of rMSNs is a promising approach to reduce the cardiotoxicity of BA. To date, no study has reported BA-loaded rMSNs (BA-rMSNs). Thus, this will be the first study of its kind.

Lipophagy is a form of selective autophagy that targets lipid droplets and is essential for lipid metabolism [17]. Lipid droplets are engulfed by autophagosomes and transported to lysosomes, where they are degraded, supplying tumor cells with energy to maintain cellular homeostasis. Some studies have demonstrated that BAs regulate autophagy; however, whether and how BAs affect lipophagy still needs to be elucidated. Thus, this study hypothesized that BA-rMSNs increase the tumor-targeting ability of BA-rMSNs and reduce their accumulation in the heart, thereby alleviating BA-mediated cardiotoxicity. Additionally, this study evaluated whether lipophagy and lipid metabolism play roles in the anticarcinoma activity of BA-rMSNs.

Materials and methods

HCT 116 and HT-29 cells were obtained from the China Center for Type Culture Collection (Shanghai, China). McCoy's 5 A medium (Gibco, New York, USA, code 16600082) along with 10% fetal bovine serum (AusGeneX, Gold Coast, Australia, code FBS500-S) and 1% penicillin–streptomycin were used to culture both cell lines (Gibco, New York, USA, code 15140122). Cetyltrimethylammonium bromide (CTAB, code H108983), ammonium hydroxide (NH_3H_2O, code A112077) and tetraethyl orthosilicate (TEOS, code T110596) were obtained from Aladdin (Shanghai, China). Bufalin (BA) was purchased from Selleck (Houston, USA, code S78213) and dissolved in dimethyl sulfoxide (DMSO) or acetone. Chloroquine (CQ) was obtained from Sigma–Aldrich (St. Louis, MO, USA; code C6628) and was dissolved in phosphate-buffered saline (PBS).

Synthesis and characterization of the rMSN

To synthesize rod-shaped mesoporous silica nanoparticles (rMSNs), 0.21 g of CTAB was mixed with 870 µL of NH_3H_2O and 54 mL of deionized water (ddH_2O) and stirred for one hour. Then, 468 µL of TEOS was added to the above mixture and stirred for another 4 h, resulting in the formation of rMSNs. To remove CTAB, the rMSNs were subsequently suspended in an ethanol solution containing hydrochloric acid (HCl) and stirred overnight at 60 °C, and the final product was obtained after washing with ethanol three times. The size of the rMSN was evaluated with a Zetatronix 919 instrument (Opptronix, Shanghai, China). The morphology was observed via transmission electron microscopy (HT7800 TEM, Hitachi, Tokyo, Japan) and a scanning electron microscope (Sigma 300 SEM, Carl Zeiss, Oberkochen, Germany). The elemental structure of the rMSN was examined via X-ray photoelectron spectroscopy (XPS) on a Thermo Fisher ESCALAB Xi+ (Waltham, MA, USA) [18, 19].

To load BA in the rMSN, BA was dissolved in acetone to obtain a 5 mg/mL BA acetone solution and mixed with the rMSN suspension at different mass ratios of rMSN to BA, such as 5:1, 4:1, 3:1, 2:1, and 1:1, for 24 h. After evaporating the solvent and washing the precipitate three times with PBS, BA-rMSNs were obtained. The loading capacity and encapsulation efficiency of BA were measured as reported previously [20]. An in vitro

BA release study was performed in PBS (pH 6.8), which simulates the tumor microenvironment, to determine the BA release profile from BA-rMSNs. Briefly, the BA-rMSN suspension was added to a dialysis bag (MWCO: 8–14 kDa), stirred and incubated at 37 °C with 25 mL of pH 6.8 PBS at 150 rpm for 72 h. At predetermined time points, 1 mL of the medium was collected, and fresh pH 6.8 PBS of the same volume was added. The BA absorbance was determined at 300 nm with the help of a multimode reader (Synergy LX BioTek, Winooski, USA). Fourier transform infrared (FTIR) spectra of BA, rMSN and BA-rMSN were obtained from 4000 to 400 cm^{-1} by a Nicolet iS5 analyzer (Thermo Fisher Scientific, Inc. Waltham, MA, USA) [21].

Subcutaneous xenograft model

Male BALB/c nude mice aged six weeks were obtained from Guangdong Medical Laboratory Animal Center (Guangzhou, China) and fed standard chow and water for one week. The local animal care committee (No. TOP-IACUC-2023-0318) approved the animal experiments. To evaluate the distribution of BA-rMSNs in vivo, a subcutaneous xenograft model was developed. Briefly, 5×10^6 HCT 116 cells were injected subcutaneously into the right flank of nude mice.

To evaluate drug cardiotoxicity, BALB/c nude mice were treated with 1 mg/kg BA or 1 mg/kg BA-rMSN, and electrocardiography (ECG) signals were acquired via a signal acquisition instrument (Yuyan Instruments, Shanghai, China). After the mice were treated for 7 days, blood samples were collected, and the creatine kinase (CK), α-hydroxybutyrate dehydrogenase (α-HBDH) and lactate dehydrogenase (LDH) levels were measured by CK (code A032), LDH (code A020), and α-HBDH (code E005) from Nanjing Jiancheng Bioengineering Institute (Nanjing, China). To investigate the distribution of the nanoparticles, IR783 (Aladdin, Shanghai, China, code I157644) or IR783-labeled BA-rMSNs were injected into the mice. The nanoparticles were examined at different time points via an in vivo imaging instrument (Biolight Biotechnology, Guangzhou, China).

Knockdown of autophagy-related 10 (ATG10)

Previous studies have demonstrated that ATG10 plays a key role in regulating autophagy and promoting cell viability in colorectal cancer [22, 23]. Thus, this study targeted ATG10 and investigated whether inhibiting lipophagy through ATG10 knockdown via shRNA would reduce the viability of colon cancer cells. Short hairpin RNA (shRNA) targeting ATG10 (shATG10 #1 and #2) with a negative control (NC) was purchased from GeneChem (Shanghai, China). In accordance with the instructions, 293T cells were transfected with shRNA plasmids and pVSVG, pMDL, and pRev (helper vectors) at a volume ratio of 5:3:2 via Liposomal Transfection Reagent (Hieff Trans®, Yeasen, Shanghai, China; code 40802ES) to produce the corresponding lentivirus. The virus-containing supernatant was subsequently collected and used to infect colon cancer cells with polybrene. Puromycin (2.5 μg/mL) was used to select stable cell lines.

Evaluating cell viability and proliferation

To assess cell viability, 4×10^3 HCT 116 and HT-29 cells per well were seeded into 96-well plates. Forty-eight hours later, the media were replaced with fresh media containing PBS (sham) or BA-rMSNs at different concentrations of BA (0.05, 0.1, 1, 10 and 100 μM). After incubation for another 48 h, a cell counting kit-8 (CCK-8) was used, and the optical density was measured at 450 nm with a Synergy LX multimode reader (BioTek, Winooski, USA). To investigate the antiproliferative activity of BA-rMSNs, cells at a density of 4×10^3/well were cultured in 96-well plates for 48 h. HCT 116 cells were treated with sham or 1 μM or 5 μM BA-rMSN, whereas HT-29 cells were treated with sham or 0.1 μM or 0.5 μM BA-rMSN for 48 h. Tumor cell proliferation was detected via quantification of the 5-ethynyl-2'-deoxyuridine (EdU) incorporation via the Click-iT™ EdU Cell Proliferation Kit (Thermo Fisher Scientific, Inc. Waltham, MA, USA; code C10337), and the results were visualized with a fluorescence microscope (Axio Vert. A1, Carl Zeiss, Oberkochen, Germany).

Evaluating cell death

To examine apoptosis, cells at a density of 2.5×10^5/well were seeded in a 6-well plate. HCT116 cells were treated with sham, 1 μM BA-rMSN, 5 μM BA-rMSN or 25 μM CQ, and HT-29 cells were treated with sham, 0.1 μM BA-rMSN, 0.5 μM BA-rMSN or 25 μM CQ for a period of 48 h. The percentage of apoptotic cells was quantified via a flow cytometer system (NovoCyte Agilent, Santa Clara, USA) and an Annexin V-APC/PI apoptosis kit (Elabscience, Houston, USA). In addition, a calcein-AM/PI double stain kit (Yeasen, Shanghai, China) was used to assess cell death.

Evaluating lipophagy

To measure the levels of lipid droplets, cells at a density of 3×10^4/well were seeded per well in 24-well plates and treated with Sham, 0.1 μM BA-rMSN, 1 μM BA-rMSN, or 25 μM CQ for 48 h. Oil red O staining solution and Nile red solution were used to stain the lipid droplets (Solarbio, Beijing, China; codes G1260 and G1264).

To evaluate lipophagy, both cell lines were seeded in 6-well plates at a density of 2.5×10^5/well. HCT116 cells were treated with sham, 1 μM BA-rMSN or 25 μM CQ, and HT-29 cells were treated with sham, 0.1 μM

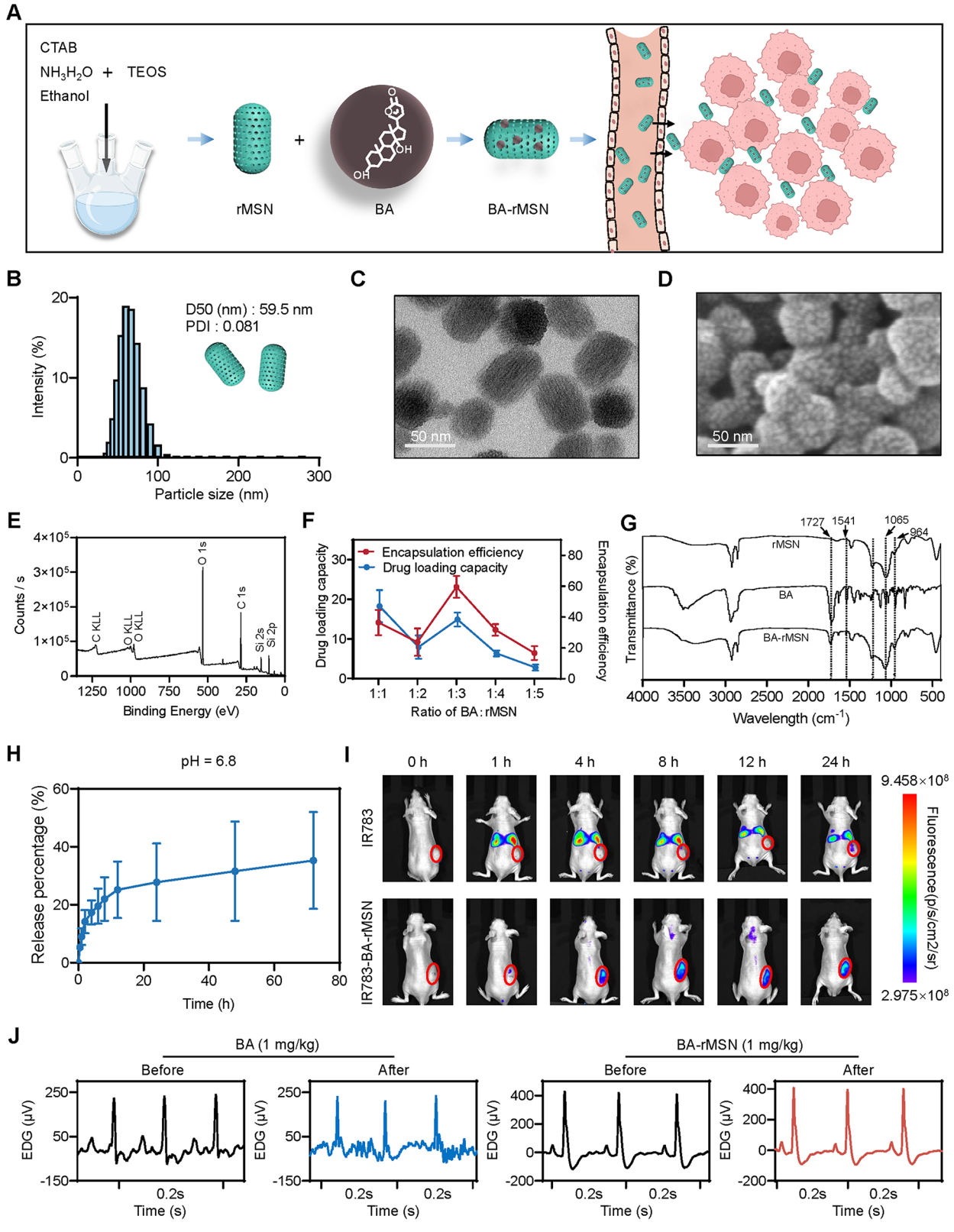

Fig. 1 (See legend on next page.)

(See figure on previous page.)

Fig. 1 Synthesis and characterization of BA-rMSNs. (**A**) CTAB, NH_3H_2O, and TEOS were used to synthesize rMSNs; subsequently, BA was loaded into the rMSNs. (**B**) The median diameter (D50) of the BA-rMSNs was 59.5 nm, and the polydispersity index (PDI) was 0.081, indicating that the rMSNs had a uniform particle size distribution. (**C**) TEM demonstrated that the BA-rMSNs had a rod-shaped morphology. (**D**) SEM image showing a rod-shaped morphology with porosity. (**E**) XPS spectrum analysis demonstrated the elemental composition of the rMSN. (**F**) The drug loading capacity and encapsulation efficiency indicated that 1:3 was the optimal ratio of BA to rMSN. (**G**) FTIR spectroscopy was used to analyze the chemical bonds and functional groups in the rMSN, BA, and BA-rMSN. (**H**) The drug release rate of BA-rMSNs was measured in pH 6.8 PBS. (**I**) In vivo, fluorescence images proved that the rMSN enhanced the tumor-targeting ability of BA. (**J**) An electrocardiogram revealed that BA caused cardiotoxicity, whereas rMSNs decreased BA-mediated toxicity

BA-rMSN or 25 μM CQ for 48 h. Western blotting (WB) was performed as previously reported [24] via the following antibodies: anti-LC3 (code #12741, dilution: 1000×), anti-P-PI3K (code #4228, dilution: 1000×), anti-T-PI3K (code #4225), anti-P-AKT (code #9271, dilution: 1000×) and anti-T-AKT (code #9272, dilution: 1000×) antibodies obtained from Cell Signaling Technology (Danvers, MA, USA). Anti-p62 (code #ab109012, dilution: 10000×), anti-P-mTOR (code #ab109268, 1000×) and anti-T-mTOR (code #ab2732, 2000×) antibodies from Abcam (Cambridge, UK) were used. An anti-β-actin antibody (Sigma–Aldrich St. Louis, USA, code A3854, dilution: 50000×) was used.

Statistical analysis

GraphPad Prism (GraphPad Software 8.0.1; San Jose, CA, USA) was used to perform all the statistical analyses. The results are shown as the median with 95% confidence intervals. The Mann−Whitney rank-sum test was employed, and the Bonferroni correction was employed for multiple comparisons. The significance level was set at $P=0.05$/the number of meaningful comparisons.

Results

Formulation and characterization of BA-rMSNs

The sol–gel method was employed to formulate rMSNs (Fig. 1A). The rMSN was approximately 60 nm in diameter (Fig. 1B). TEM images revealed that the rMSNs exhibited a rod-shaped morphology with porous channels (Fig. 1C), which is consistent with the SEM results (Fig. 1D). For further elemental analysis of the rMSN, XPS was conducted, as depicted in Fig. 1E. XPS analysis revealed Si atoms with binding energies of 153.8 eV (Si 2 s) and 102.9 eV (Si 2p). Moreover, C 1 s and O 1 s peaks were detected at binding energies of 532.1 eV and 284.8 eV, respectively. These results confirmed the successful formation of mesoporous silica nanoparticles. The drug encapsulation efficiency and loading capacity were evaluated to determine the optimal ratio of rMSN to bufalin (BA). A mass ratio of 1:3 (BA to rMSN) resulted in higher encapsulation efficiency and drug loading capacity than the other ratios did (Fig. 1F). Therefore, this ratio was used to develop BA-loaded rMSNs (BA-rMSNs).

The characteristic FTIR peaks of the mesoporous silica nanoparticles are located at 1065 cm^{-1} and 964 cm^{-1} and correspond to the asymmetric stretching vibrations of Si–O–Si and the bending vibrations of Si–OH bonds, respectively (Fig. 1G). This indicates the presence of silanol groups on the surface of the rMSN. The peaks at 1541 cm^{-1} and 1727 cm^{-1} were derived from the C=C stretching vibration and the lactone bond of BA, which appear weakly in the spectra of BA-rMSNs. In addition, the characteristic peaks of Si–O–Si and Si–OH bonds at 1073 cm^{-1} and 964 cm^{-1} were observed, indicating that BA was successfully encapsulated within the pores of the rMSN. The drug release behavior of rMSN-loaded BA was studied at pH 6.8, and the results demonstrated that the drug release rate was approximately 35% (Fig. 1H). Thus, rMSNs are a suitable delivery system for the release of anticancer drugs in weakly acidic tumor tissues, thereby promoting drug accumulation and enhancing the therapeutic effect.

A biodistribution study of BA-rMSNs via in vivo fluorescence imaging revealed that rMSNs enhanced the accumulation of BA in tumors (Fig. 1I). To detect toxicity, electrocardiograms were performed to determine whether BA-rMSNs mitigate cardiotoxicity. After the administration of 1 mg/kg BA, inverted T waves were examined via electrocardiography, which revealed cardiotoxicity. In contrast, the same 1 mg/kg BA-rMSN had no cardiotoxic effects (Fig. 1J). CK, LDH, and α-HBDH are key biomarkers for detecting myocardial infarction. After BA was administered to the mice, there was a slight increase in the levels of these enzymes. Although treatment with BA-rMSNs resulted in a decrease in CK, LDH, and α-HBDH levels, these changes were not statistically significant (Fig. S1).

BA-rMSNs inhibit proliferation and induce apoptosis

To evaluate the optimal dose of BA-rMSNs for in vitro study, both cell lines were treated with various concentrations of BA-rMSNs for 48 h (Fig. 2A-B). BA-rMSNs markedly reduced cell viability in both cell lines in a dose-dependent fashion. The half-maximal inhibitory concentration (IC_{50}) value for HCT 116 was 4.69 μM, and that for HT-29 cells was 0.26 μM (Fig. 2C). To assess the antiproliferative activity of BA-rMSNs, an EdU assay was performed. In both cell lines, BA-rMSNs presented significantly reduced green fluorescence, indicating decreased DNA replication compared with that of the controls (Fig. 2D-E). These results suggest that

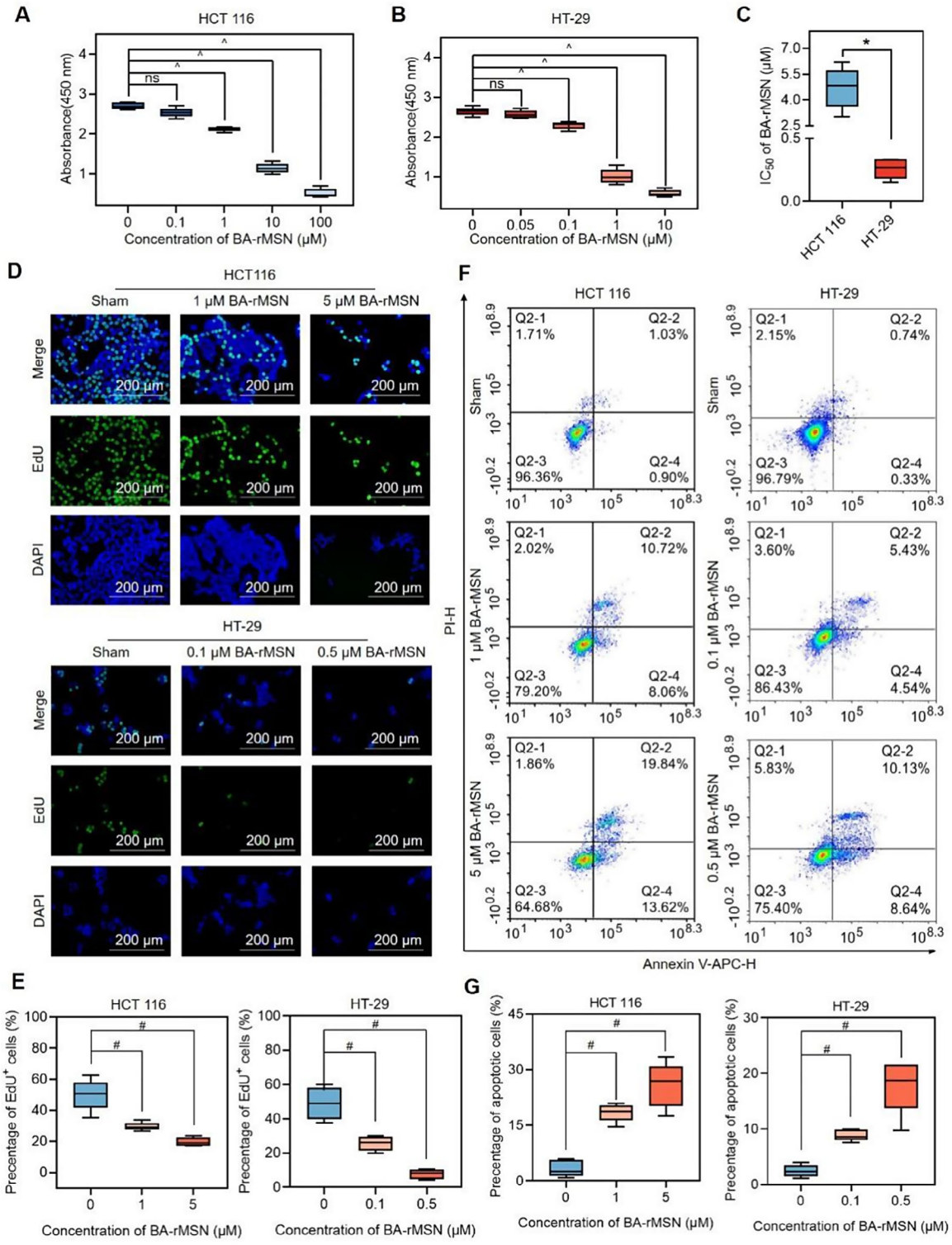

Fig. 2 BA-rMSNs inhibit proliferation and induce cell death. (**A**) HCT 116 cells and (**B**) HT-29 cells were treated with PBS or different dosages of BA-rMSNs for 48 h. The results of the CCK8 assay revealed that BA-rMSNs significantly inhibited the viability of these cells. (**C**) The IC_{50} values indicated that, compared with HCT 116 cells, HT-29 cells were more sensitive to BA-rMSNs. Representative fluorescence microscopy images (**D**) and quantitative analysis of EdU (**E**) confirmed that BA-rMSNs significantly inhibited proliferation. (**F**) Annexin V-APC/PI staining revealed that BA-rMSNs increased the percentages of Annexin V-APC+/PI- (early apoptotic) cells and Annexin V-APC+/PI+ (late apoptotic) cells. (**G**) Quantification of the percentage of apoptotic HCT 116 and HT-29 cells. and E-G. ns indicates no significance, * indicates a *P* value lower than 0.05, # indicates a *P* value lower than 0.0167, and ^ indicates a *P* value lower than 0.0125, determined via the Mann–Whitney U test. IC_{50}: half-maximal inhibitory concentration

BA-rMSNs substantially inhibit colon cancer cell proliferation. Additionally, Annexin V and PI staining analysis demonstrated that BA-rMSNs significantly increased the ratio of Annexin V-APC/PI-positive cells (Fig. 2F-G). These findings confirmed that BA-rMSNs induced both early and late apoptosis in these cells.

BA-rMSNs impair lipophagy in colon cancer

Lipid droplet density was determined via oil red O and Nile red staining to evaluate the relationship between BA-rMSNs and lipophagy. Oil red O staining revealed that 1 μM BA-rMSN and 0.1 μM BA-rMSN led to the accumulation of lipid droplets in HCT 116 and HT-29 cells, respectively (Fig. 3A). Nile red staining revealed a significant increase in red fluorescence signals in BA-rMSN-treated cells compared with those in sham-treated cells (Fig. 3B-C), suggesting that BA-rMSNs inhibited the degradation of lipid droplets. To further investigate this relationship, the levels of LC3 and p62, two common lipophagy substrates, were also determined. BA-rMSNs increased the accumulation of LC3 and p62 (Fig. 3D), suggesting that BA-rMSNs blocked lipophagy.

BA-rMSNs fight against colon cancer by suppressing lipophagy

To determine whether lipophagy plays a role in the antitumor activity of BA-rMSNs, lipophagy was blocked by chloroquine (CQ), an inhibitor of lipophagy (Fig. 4A). Nile red staining demonstrated that blocking lipophagy significantly increased the accumulation of lipid droplets (Fig. 4B-C). Annexin V-APC/PI staining analysis confirmed that the suppression of lipophagy by CQ induced considerable cell death (Fig. 4D and Fig. S2). These findings demonstrated that blocking lipophagy impaired the apoptosis induced by CQ.

To verify these observations, ATG10, which prompts the early stage of autophagic flux, was knocked down by shRNA lentivirus, and the level of lipid droplets was determined. WB revealed that the knockdown of ATG10 by shATG10 #2 reduced the level of ATG10 and increased the levels of LC3 and p62 (Fig. 5A). Therefore, shATG10 #2 was used for the following study. Compared with the negative control, ATG10 knockdown markedly increased the number of lipid droplets (Fig. 5B-C). To investigate whether lipophagy induces cell growth, cell death was determined via calcein-AM/PI double-staining in both cell lines (Fig. 5D-E). Compared with that in the sham-treated cells, the percentage of PI-positive cells was significantly greater in the ATG10-knockdown cells. These findings support the hypothesis that BA-rMSNs inhibit tumor growth by blocking lipophagy.

Discussion

BA is a promising agent for treating gastrointestinal cancers, such as stomach, colorectal, and pancreatic carcinomas [20, 25, 26]. However, its limitations include poor water solubility, short half-life, and strong cardiotoxic effects. To overcome these drawbacks, BA-loaded rMSNs have been developed. In vitro studies indicated that BA-rMSNs blocked lipophagy and therefore induced colon cancer cell apoptosis. In vivo studies revealed that BA-rMSNs significantly decreased the mortality rate and enhanced tumor targeting. These results are clinically relevant. For example, compared with BA, BA-loaded rMSNs significantly decrease cardiotoxicity and exhibit anticarcinoma activity. Thus, the present study suggests that BA-loaded rMSNs constitute a promising strategy for fighting cancer, which needs to be evaluated in a clinical study.

The HCT 116 cell line, derived from the colon of an adult male with colon cancer, exhibited positive expression of transforming growth factor beta 1 (TGF-β1) and beta 2 (TGF-β2). The HT-29 cell line, characterized by its epithelial morphology, was isolated from a Caucasian female patient with colorectal adenocarcinoma and expresses oncogenes such as c-myc, K-ras, and H-ras. To determine whether these molecular differences affect the anticancer activity of BA-rMSNs, we assessed their efficacy in both the HCT 116 and HT-29 cell lines. The results demonstrated that BA-rMSNs significantly reduced cell viability and induced cell death in both lines, with IC50 values of 4.69 μM for HCT 116 and 0.26 μM for HT-29. Given that HCT 116 is positive for TGF-β1 and TGF-β2, these factors may contribute to the chemoresistance of HCT 116 to BA. Further investigations are needed to explore this potential mechanism in future studies.

Previous studies have also developed various BA-loaded nanoparticles and evaluated their antitumor effects [27–29]. For example, Xu et al. developed multifunctional albumin submicrospheres via coaxial electrospray technology to codeliver BA and nintedanib. These microspheres were modified with biguanide and ursodeoxycholic acid to enhance their tumor-targeting properties and antitumor effects [29]. This carrier significantly reduced the volume and weight of the tumors in vivo. However, the advantages of these nanoparticles in reducing BA-induced cardiotoxicity have not been reported. Additionally, peptide and protein drugs have high molecular weights and poor stability. These drugs are easily degraded by proteolytic enzymes in the gastrointestinal tract [27]. Ning et al. also demonstrated that MSNs offer substantial benefits in improving the antitumor efficacy of BA. Compared with lenvatinib or bufacillin alone, spherical MSNs codelivering bufacillin and lenvatinib notably decreased the tumor burden

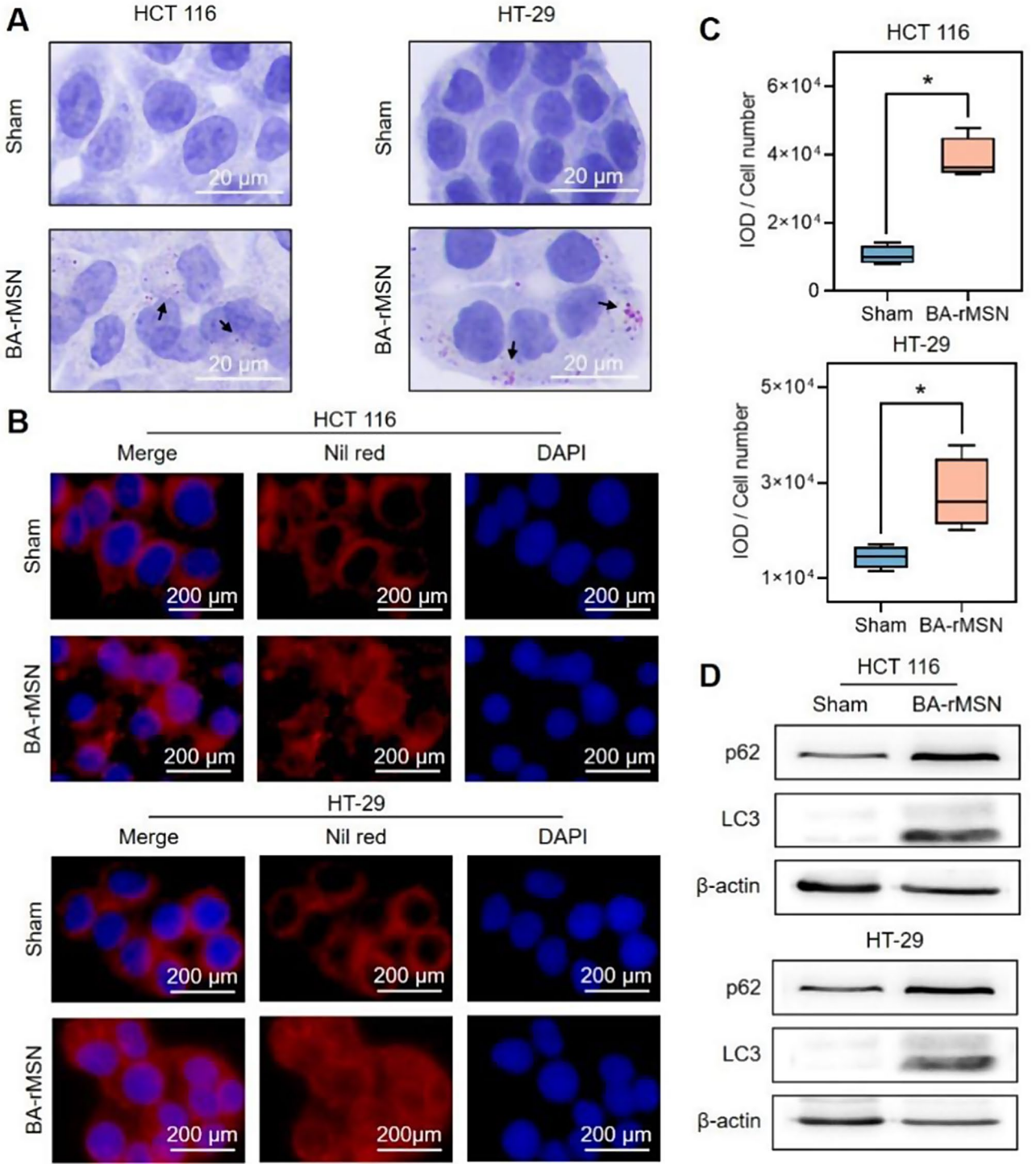

Fig. 3 BA-rMSNs blocked lipophagy. (**A**) Oil red O staining and (**B**) Nile red staining demonstrated that BA-rMSNs increased the accumulation of lipid droplets. (**C**) Quantitative analysis of Nile red staining results in HCT 116 and HT-29 cells revealed an increase in lipid droplet accumulation. (**D**) Western blot analysis revealed that BA-rMSNs increased the levels of p62 and LC3, indicating the inhibition of lipophagy. $N = 4$ for B. * indicates a P value lower than 0.05, which was determined by the Mann–Whitney U test. IOD: Integrated optical density

[30]. As previously mentioned, compared with other shapes of MSNs, rMSNs exhibit superior internalization efficiency and greater mucus and intestinal epithelial barrier penetrability [16], and currently, no study has assessed the advantages of BA-loaded rMSNs. In this study, BA-rMSNs were developed, and their effects were evaluated via electrocardiograms (ECGs) and several blood biomarkers associated with myocardial infarction.

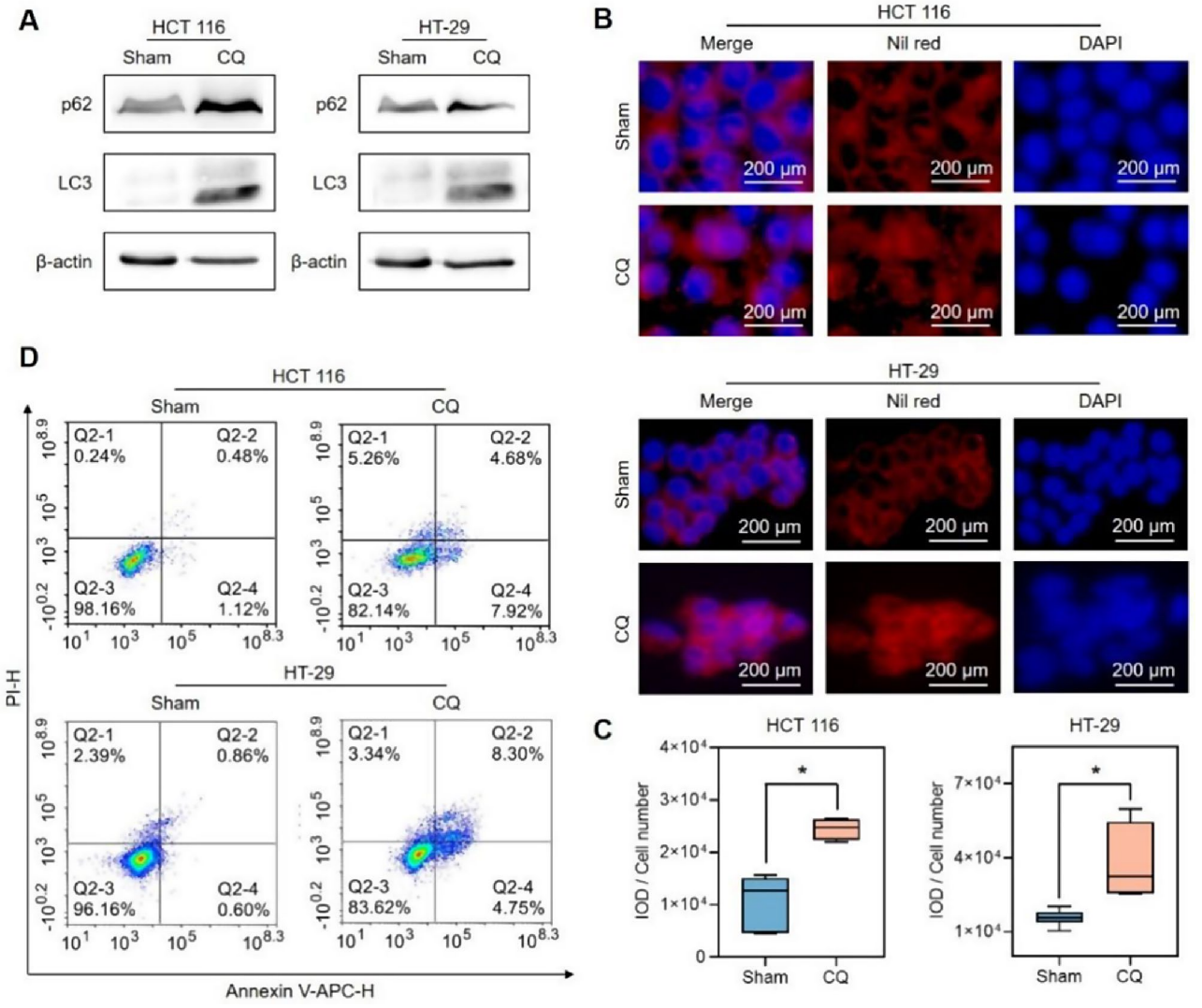

Fig. 4 The inhibition of lipophagy by CQ led to apoptosis. (**A**) CQ increased the levels of p62 and LC3, which indicated that CQ blocked lipophagy. (**B**) Nile red staining suggested that CQ significantly increased the level of lipid droplets. (**C**) Quantitative fluorescence intensity of Nile red in HCT 116 and HT-29 cells after treatment with 25 μM CQ. (**D**) Annexin V-APC/PI staining confirmed that blocking lipophagy induced cell death. $N = 4$ for B. * indicates a P value lower than 0.05, which was determined by the Mann–Whitney U test

Significant changes in cardiac function were observed in the ECG after treatment. However, only slight decreases in CK, LDH, and α-HBDH were observed when BA-rMSNs were compared with BA. BA is a digoxin analog that causes arrhythmias, and electrocardiograms are the most common method for diagnosing arrhythmias, while CK, LDH and α-HBDH serve as biomarkers of myocardial damage. Therefore, no notable difference was observed in these biomarkers between the mice treated with BA or BA-rMSNs.

Lipophagy plays a crucial role in the pathophysiology of colon cancer [31]. Lipid droplets can be degraded by lipophagy to provide necessary nutrients, such as free fatty acids, to support the rapid proliferation and growth of tumors [32]. Lipophagy and autophagy share the same molecular regulatory pathway [33]. Robert A Masuda et al. reported increased expression of LC3, an indicator of autophagy, in 3T3-L1 cells treated with isothiocyanate sulforaphane (SFN). Immunofluorescence demonstrated that LC3 colocalized with lipid droplets in 3T3-L1 cells. These findings suggest that SFN induces lipophagy. Furthermore, evaluation of the mechanism revealed that SFN induces lipophagy via AMPK-mTOR-ULK1 pathway activation, resulting in a reduction in lipid droplets. Taken together, these results imply that this signaling pathway has a role in lipophagy [34]. In addition, some studies reported that stimulator of interferon response cGAMP interactor 1 (STING1), lysosomal associated membrane protein 2 (LAMP-2), and forkhead box O1

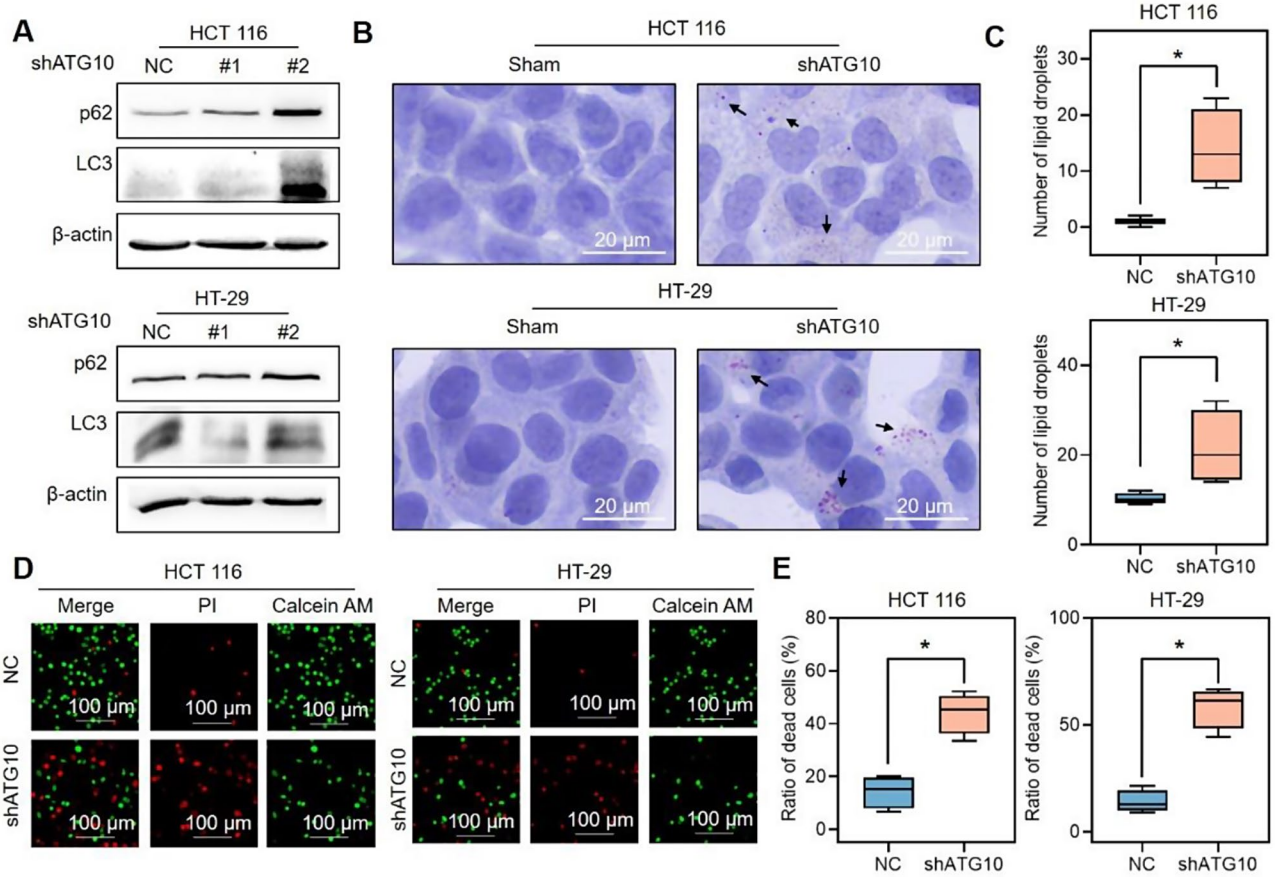

Fig. 5 Lipophagy contributes to cell growth. (**A**) shATG10 was used to inhibit lipophagy. (**B**) Blocking lipophagy significantly increased the accumulation of lipid droplets, as shown by Oil Red O staining. (**C**) Quantitative analysis of the Oil red O staining results. (**D**) Inhibition of lipophagy by shATG10 significantly induced cell death. (**E**) Quantitative analysis of the ratio of dead cells by calcein AM/PI staining. *N* = 4 for B and C. * indicates a *P* value lower than 0.05, which was determined by the Mann–Whitney U test

(FoxO1), the common regulators of autophagy, also contribute to regulating lipophagy [35–37].

The results of the present study demonstrated that p62 and LC3 expression increased and that lipid droplets accumulated following BA-rMSN treatment. Moreover, the relationship between mTOR and lipophagy was explored in the present study. BA-rMSNs increased the level of P-mTOR (Fig. S3A), suggesting that BA-rMSNs reduce lipophagy by activating the mTOR signaling pathway. Although proteins associated with the mTOR pathway, such as PI3K and AKT, are known to regulate autophagy, BA-rMSNs reduced P-PI3K and P-AKT expression (Fig. S3B). These findings indicate that BA-rMSNs regulate autophagy through a mechanism that is not dependent on PI3K/AKT.

Strengths and limitations

This study highlights for the first time the potential of BA-rMSNs in treating colon cancer. The unique properties of rMSNs, including their rod-like shape and superior drug loading capacity, make them suitable for the delivery of bufalin to target the tumor site, thereby reducing cardiac distribution and cardiotoxicity. Mechanistically, the present study demonstrated that BA-rMSNs inhibit the degradation of lipid droplets by blocking lipophagy, further disrupting cellular homeostasis and inducing cell death. These findings lay a solid foundation for its clinical application, which is expected to improve the clinical outcomes of patients with colon cancer. However, several limitations remain. First, the aspect ratio of BA-rMSNs was not optimized in the present study. The aspect ratio is an essential parameter for rod-shaped nanoparticles and affects the blood circulation, tumor accumulation and cell internalization efficiency of the nanoparticles. Further studies are needed to investigate which aspect ratio of the rMSN is optimal for the delivery of BA and other chemotherapeutic drugs. Currently, the safety of single-dose BA-rMSNs has been carefully evaluated, and further study is needed to investigate the safety profile of long-term administration of BA-rMSNs, including their metabolites and potential side effects. Furthermore, this study reported that BA-rMSNs blocked lipophagy.

However, how BA-rMSNs regulate lipophagy remains to be elucidated, and other lipophagy-related proteins, such as STING1, LAMP-2, and FoxO1, also need to be evaluated.

Conclusions

In conclusion, novel rod-shaped MSNs were developed to deliver BA to enhance its antitumor effect and reduce cardiotoxicity. A mechanistic study revealed that BA-rMSNs blocked lipophagy.

Abbreviations

BA	Bufalin
MSN	Mesoporous Silica Nanoparticle
rMSNs	Rod-shaped Mesoporous Silica Nanoparticles
BA-rMSNs	Bufalin-loaded Rod-Shaped Mesoporous Silica Nanoparticles
PI3Ks	Phosphoinositide 3-Kinase
AKT	Protein Kinase B
mTOR	Mammalian Target of Rapamycin
EPR	Enhanced Permeability and Retention
CTAB	Cetyltrimethylammonium Bromide
NH_3H_2O	Ammonium Hydroxide
TEOS	Tetraethyl Orthosilicate
DMSO	Dimethyl Sulfoxide
CQ	Chloroquine
PBS	Phosphate-Buffered Saline
TEM	transmission Electron Microscopy
SEM	Scanning Electron Microscope
XPS	X-ray Photoelectron Spectroscopy
FTIR	Fourier Transform Infrared
ECG	Electrocardiography
CK	Creatine Kinase
LDH	Lactate Dehydrogenase
α-HBDH	α-Hydroxybutyrate Dehydrogenase
ATG10	Autophagy-Related 10
EdU	5-Ethynyl-2′-Deoxyuridine
LC3	Microtubule-Associated Protein 1 A/1B Light Chain 3B
p62	p62/SQSTM1
D50	Median Diameter
IOD	Integrated Optical Density
SFN	Isothiocyanate Sulforaphane
STING1	Stimulator of Interferon Response cGAMP Interactor 1
LAMP-2	Lysosomal Associated Membrane Protein 2
FoxO1	Forkhead Box O1
TGF-β1	Transforming Growth Factor Beta 1
TGF-β2	Transforming Growth Factor Beta 2

Supplementary Information

The online version contains supplementary material available at https://doi.org/10.1186/s12944-024-02301-y.

Supplementary Material 1

Acknowledgements

The data are available from the corresponding author upon reasonable request.

Author contributions

Perform the study: YF. Write manuscript: YF, XZ & ZI. Revise the manuscript: YF, WZ & XL. Data curation: ZL, WZ & QL. Formal analysis: WZ, XL & HD. Project administration: PL. Funding acquisition: PG & PL. Study design: XZ. All the authors have approved the final version of the manuscript.

Funding

This work was supported by the Shenzhen Key Medical Discipline Construction Fund & Sanming Project of Medicine in Shenzhen (SZSM202111002), the Shenzhen Higher Education Stability Support Plan (Grant number: 20231121221806001), the Shenzhen Science and Technology Program (GJHZ20220913143005010) and the Medical Engineering Interdisciplinary Research Foundation of Shenzhen University (2023YG019).

Data availability

No datasets were generated or analysed during the current study.

Declarations

Ethical approval

The animal experiments were approved by the local animal care committee (No. TOP-IACUC-2023-0318).

Consent for publication

All the authors read the final version and agree to publish it.

Competing interests

The authors declare no competing interests.

Received: 2 June 2024 / Accepted: 16 September 2024
Published online: 27 September 2024

References

1. Zhang XB, Fan YB, Jing R, Getu MA, Chen WY, Zhang W, Dong HX, Dakal TC, Hayat A, Cai HJ, et al. Gastroenteropancreatic neuroendocrine neoplasms: current development, challenges, and clinical perspectives. Mil Med Res. 2024;11:35.
2. Bray F, Laversanne M, Sung H, Ferlay J, Siegel RL, Soerjomataram I, Jemal A. Global cancer statistics 2022: GLOBOCAN estimates of incidence and mortality worldwide for 36 cancers in 185 countries. CA Cancer J Clin. 2024;74:229–63.
3. Xie YH, Chen YX, Fang JY. Comprehensive review of targeted therapy for colorectal cancer. Signal Transduct Target Ther. 2020;5:22.
4. Soumoy L, Ghanem GE, Saussez S, Journe F. Bufalin for an innovative therapeutic approach against cancer. Pharmacol Res. 2022;184:106442.
5. Chen J, Wang H, Jia L, He J, Li Y, Liu H, Wu R, Qiu Y, Zhan Y, Yuan Z, et al. Bufalin targets the SRC-3/MIF pathway in chemoresistant cells to regulate M2 macrophage polarization in colorectal cancer. Cancer Lett. 2021;513:63–74.
6. Ko RJ, Greenwald MS, Loscutoff SM, Au AM, Appel BR, Kreutzer RA, Haddon WF, Jackson TY, Boo FO, Presicek G. Lethal ingestion of Chinese herbal tea containing Ch'an su. West J Med. 1996;164:71–5.
7. Jafari S, Derakhshankhah H, Alaei L, Fattahi A, Varnamkhasti BS, Saboury AA. Mesoporous silica nanoparticles for therapeutic/diagnostic applications. Biomed Pharmacother. 2019;109:1100–11.
8. Tarn D, Ashley CE, Xue M, Carnes EC, Zink JI, Brinker CJ. Mesoporous silica nanoparticle nanocarriers: biofunctionality and biocompatibility. Acc Chem Res. 2013;46:792–801.
9. Chung TH, Wu SH, Yao M, Lu CW, Lin YS, Hung Y, Mou CY, Chen YC, Huang DM. The effect of surface charge on the uptake and biological function of mesoporous silica nanoparticles in 3T3-L1 cells and human mesenchymal stem cells. Biomaterials. 2007;28:2959–66.
10. Slowing I, Trewyn BG, Lin VS. Effect of surface functionalization of MCM-41-type mesoporous silica nanoparticles on the endocytosis by human cancer cells. J Am Chem Soc. 2006;128:14792–3.
11. Kim JS, Yoon TJ, Yu KN, Noh MS, Woo M, Kim BG, Lee KH, Sohn BH, Park SB, Lee JK, Cho MH. Cellular uptake of magnetic nanoparticle is mediated through energy-dependent endocytosis in A549 cells. J Vet Sci. 2006;7:321–6.
12. Kortesuo P, Ahola M, Karlsson S, Kangasniemi I, Yli-Urpo A, Kiesvaara J. Silica xerogel as an implantable carrier for controlled drug delivery–evaluation of drug distribution and tissue effects after implantation. Biomaterials. 2000;21:193–8.
13. Falsafi SR, Rostamabadi H, Assadpour E, Jafari SM. Morphology and microstructural analysis of bioactive-loaded micro/nanocarriers via microscopy techniques; CLSM/SEM/TEM/AFM. Adv Colloid Interface Sci. 2020;280:102166.
14. Li Q, Liu W, Liu K, Dong Z, Kong W, Lu X, Wei Y, Wu W, Yang J, Qi J. The role of nanoparticle morphology on enhancing delivery of Budesonide for Treatment of Inflammatory Bowel Disease. ACS Appl Mater Interfaces. 2024;16:33081–92.

15. Wang F, Li J, Tang X, Huang K, Chen L. Polyelectrolyte three layer nanoparticles of chitosan/dextran sulfate/chitosan for dual drug delivery. Colloids Surf B Biointerfaces. 2020;190:110925.
16. Banerjee A, Qi J, Gogoi R, Wong J, Mitragotri S. Role of nanoparticle size, shape and surface chemistry in oral drug delivery. J Control Release. 2016;238:176–85.
17. Zhang X, Kumstel S, Jiang K, Meng S, Gong P, Vollmar B, Zechner D. LW6 enhances chemosensitivity to gemcitabine and inhibits autophagic flux in pancreatic cancer. J Adv Res. 2019;20:9–21.
18. Wibowo FR, Saputra OA, Lestari WW, Koketsu M, Mukti RR, Martien R. pH-Triggered drug release controlled by poly(Styrene Sulfonate) Growth Hollow Mesoporous silica nanoparticles. ACS Omega. 2020;5:4261–9.
19. Morsi RE, Mohamed RS. Nanostructured mesoporous silica: influence of the preparation conditions on the physical-surface properties for efficient organic dye uptake. R Soc Open Sci. 2018;5:172021.
20. Zhang W, Fan Y, Zhang J, Shi D, Yuan J, Ashrafizadeh M, Li W, Hu M, Abd El-Aty AM, Hacimuftuoglu A, et al. Cell membrane-camouflaged bufalin targets NOD2 and overcomes multidrug resistance in pancreatic cancer. Drug Resist Updat. 2023;71:101005.
21. Xu Y, Tang L, Chen P, Chen M, Zheng M, Shi F, Wang Y. Tumor-targeted delivery of bufalin-loaded modified albumin-polymer hybrid for enhanced Antitumor Therapy and attenuated Hemolysis Toxicity and Cardiotoxicity. AAPS PharmSciTech. 2021;22:137.
22. Sun W, Li J, Zhou L, Han J, Liu R, Zhang H, Ning T, Gao Z, Liu B, Chen X, et al. The c-Myc/miR-27b-3p/ATG10 regulatory axis regulates chemoresistance in colorectal cancer. Theranostics. 2020;10(5):1981–96.
23. Jo YK, Roh SA, Lee H, Park NY, Choi ES, Oh JH, Park SJ, Shin JH, Suh YA, Lee EK, et al. Polypyrimidine tract-binding protein 1-mediated down-regulation of ATG10 facilitates metastasis of colorectal cancer cells. Cancer Lett. 2017;385:21–7.
24. Yuan J, Zhu Z, Zhang P, Ashrafizadeh M, Abd El-Aty AM, Hacımüftüoğlu A, Linnebacher CS, Linnebacher M, Sethi G, Gong P, Zhang X. SKP2 promotes the metastasis of pancreatic ductal adenocarcinoma by suppressing TRIM21-mediated PSPC1 degradation. Cancer Lett. 2024;587:216733.
25. Chen G, Zhang H, Sun H, Ding X, Liu G, Yang F, Feng G, Dong X, Zhu Y, Wang X, et al. Bufalin targeting BFAR inhibits the occurrence and metastasis of gastric cancer through PI3K/AKT/mTOR signal pathway. Apoptosis. 2023;28:1390–405.
26. Wang H, Chen J, Li S, Yang J, Tang D, Wu W, Yu K, Cao Y, Xu K, Yin P, et al. Bufalin reverses cancer-associated fibroblast-mediated colorectal cancer metastasis by inhibiting the STAT3 signaling pathway. Apoptosis. 2023;28:594–606.
27. Pawar VK, Meher JG, Singh Y, Chaurasia M, Surendar Reddy B, Chourasia MK. Targeting of gastrointestinal tract for amended delivery of protein/peptide therapeutics: strategies and industrial perspectives. J Control Release. 2014;196:168–83.
28. Wang H, Wu J, Williams GR, Fan Q, Niu S, Wu J, Xie X, Zhu LM. Platelet-membrane-biomimetic nanoparticles for targeted antitumor drug delivery. J Nanobiotechnol. 2019;17:60.
29. Xu Y, Liu Y, Liu Q, Lu S, Chen X, Xu W, Shi F. Co-delivery of bufalin and nintedanib via albumin sub-microspheres for synergistic cancer therapy. J Control Release. 2021;338:705–18.
30. Ning Z, Zhao Y, Yan X, Hua Y, Meng Z. Flower-like Composite Material Delivery of Co-packaged Lenvatinib and Bufalin prevents the Migration and Invasion of Cholangiocarcinoma. Nanomaterials (Basel). 2022;12.
31. Assumpção JAF, Magalhães KG, Corrêa JR. The role of pparγ and autophagy in ros production, lipid droplets biogenesis and its involvement with colorectal cancer cells modulation. Cancer Cell Int. 2017;17:82.
32. Geng F, Guo D. SREBF1/SREBP-1 concurrently regulates lipid synthesis and lipophagy to maintain lipid homeostasis and tumor growth. Autophagy. 2024;20:1183–5.
33. Qin Y, Ashrafizadeh M, Mongiardini V, Grimaldi B, Crea F, Rietdorf K, Győrffy B, Klionsky DJ, Ren J, Zhang W, Zhang X. Autophagy and cancer drug resistance in dialogue: pre-clinical and clinical evidence. Cancer Lett. 2023;570:216307.
34. Masuda M, Yoshida-Shimizu R, Mori Y, Ohnishi K, Adachi Y, Sakai M, Kabutoya S, Ohminami H, Yamanaka-Okumura H, Yamamoto H, et al. Sulforaphane induces lipophagy through the activation of AMPK-mTOR-ULK1 pathway signaling in adipocytes. J Nutr Biochem. 2022;106:109017.
35. Narabayashi K, Ito Y, Eid N, Maemura K, Inoue T, Takeuchi T, Otsuki Y, Higuchi K. Indomethacin suppresses LAMP-2 expression and induces lipophagy and lipoapoptosis in rat enterocytes via the ER stress pathway. J Gastroenterol. 2015;50:541–54.
36. Liu K, Qiu D, Liang X, Huang Y, Wang Y, Jia X, Li K, Zhao J, Du C, Qiu X, et al. Lipotoxicity-induced STING1 activation stimulates MTORC1 and restricts hepatic lipophagy. Autophagy. 2022;18:860–76.
37. Lo MC, Chen JY, Kuo YT, Chen WL, Lee HM, Wang SG. Camptothecin activates SIRT1 to promote lipid catabolism through AMPK/FoxO1/ATGL pathway in C(2)C(12) myogenic cells. Arch Pharm Res. 2019;42:672–83.

Publisher's note